A bi-annual journal published by the Faculty of Science, University of Lagos, Nigeria
http://jsrd.unilag.edu.ng/index.php/jsrd

Superposed epoch analysis of relativistic electron flux depletion during moderate CIR storms

*[1]Busola Olugbon, [1]Elijah Oyedola Oyeyemi, [1]Andrew Oke-Ovie Akala and [2]Mei-Ching Hannah Fok
[1]Department of Physics, University of Lagos, Lagos, Nigeria
[2]Geospace Physics Laboratory, NASA Goddard Space Flight Center, Maryland, USA
*Corresponding author: bolugbon@unilag.edu.ng

Received 20 February 2025/Revised 10 April 2025/Accepted 11April 2025

Abstract

A superposed epoch analysis of radiation belt electron flux depletions during September 2012 - December 2018 identified 46 clear dropout events of duration ≤ 24 hours and which extended below L = 5. Of this number, 58% were associated with co-rotating interaction region (CIR) storms. The dropouts associated with CIR storms during SYM/H index ≥ - 80 nT intervals were energy dependent with depleted 1.8 MeV fluxes returning to pre-depletion levels after the storm, and true losses occurring for fluxes of higher energy electrons. However, the population of the source electrons (54 keV) increased during the same intervals while the 742 keV electrons population appeared to be driven by competing enhancement and loss processes. The highest depletion levels were recorded for electrons of energy 1.8 MeV at 4.6 ≤ L ≤ 4.9. A superposed epoch analysis showed that onset of 1.8 MeV flux depletions was triggered by substorm expansion phase and southward orientation of the field-aligned component of interplanetary magnetic field (IMF Bz). On the other hand, recovery of fluxes coincided with substorm recovery and IMF Bz northward reversal. Analysis of cosmic noise absorption data during a selected flux depletion event showed evidence of ionosperic precipitation.

Keywords: flux depletions, ionospheric precipitation, superposed-epoch analysis

---

Introduction

The launch of the Van Allen Probes (Mauk *et al.*, 2013) in September 2012 facilitated closer examination of the structure and dynamics of the radiation belts and clearer understanding of the behavior of the charged particles which constitute these belts. These charged particles are a source of damage to spacecrafts and on-board instruments, especially during geomagnetic storms when they accelerated to relativistic energies. Borovsky and Denton (2006) described the differences between co-rotating interaction region (CIR) and coronal mass ejection (CME) driven geomagnetic storms. The differences were outlined in terms of appearance of storm sudden commencement (SSC), plasma sheet density and temperature, ring current (Dst index), fluxes of relativistic electrons, ultra-low frequency (ULF) pulsations among others. For instance, CIR driven storms rarely feature the SSC signature i.e. a sudden positive excursion of the Dst index before the main phase of the storm. Furthermore, the Dst index does not dip sharply during CIR driven storms. Rather it decreases gradually over several hours to a minimum value and usually takes several days to return to pre-storm values.

The response of radiation belt particles to geomagnetic storms has been investigated over the years. Reeves et al. (2003) examined the response of 1.8 – 3.5 MeV fluxes to geomagnetic storms spanning the peak of solar cycle 23 to the peak of solar cycle 24. Their results showed that 53% of the storms caused an enhancement in fluxes of electrons in geosynchronous orbit, 19% caused a decrease in fluxes, while 28% resulted in no significant change of fluxes. Turner *et al.* (2015) investigated the response to geomagnetic storms of

various populations of radiation belt electrons at ~3 ≤ L ≤ 7. Data from September 2012 to February 2015 were analyzed and a total of 52 storms were considered. Their results for 1.5 MeV electrons at L = 6 showed that 39% of the storms resulted in an enhancement, 26% resulted in depletion, and 35% resulted in no significant change in relative levels of the pre-storm and post storm electron fluxes. They also reported that the ~ MeV electrons had the highest occurrence of depletion events which occurred mainly at L > 4 and that the peak location of these electrons after the storm remained between 4 ≤ L ≤ 5. Moya *et al.* (2017) undertook a statistical study on the effect of geomagnetic storms on relativistic electron fluxes and found that the L-shell and energy were the principal factors which determined whether an electron was energized, lost, or remained unchanged in the outer radiation belt. For enhancement of relativistic electron fluxes, it was observed that more intense storms caused the radiation belt to move inward toward the Earth. A total of 78 storms between September 2012 and June 2016 were considered and the results showed 45%, 32%, and 23% probability of enhancement, depletion, or no-change response, respectively for 1.8 MeV electrons at L = 6.

Katsavarias et al. (2019) in their statistical analysis of acceleration and loss of relativistic electrons in the outer radiation belt used electron phase space density calculations and the maximum compression of the magnetopause as indices to investigate the behavior of radiation belt electrons. Their dataset spanned September 2012 to April 2018 and 8 depletion events, as well as 20 enhancement events, during either CME or CIR driven storms were investigated. Results from the study showed that magnetopause shadowing and outward radial diffusion were primarily responsible for depletion of radiation belt electrons. Bortnik *et al.* (2006) investigated in detail a dropout event which occurred during the 20 November 2003 geomagnetic storm and reported two different dropout mechanisms dominating at high (L > 5) and lower L-shells. The high L-shell losses were attributed mainly to magnetopause shadowing, outward radial diffusion, and adiabatic losses which affected all energies indiscriminately. However, at lower L-shells losses were found to be energy dependent with ≤ 0.45 MeV electron flux losses being adiabatic whereas fluxes of ≥ 0.63MeV electrons were not adiabatic. The non adiabatic losses were reported to have been caused by electromagnetic ion cyclotron (EMIC) waves in the plasmasphere.

Superposed epoch analysis

A superposed epoch analysis of the dropouts of relativistic electron fluxes during 124 high speed stream (HSS) driven storms was presented by Borovsky and Denton (2009). Data from the multi-spacecraft Magnetospheric Plasma Analyzer showed that the dropout of relativistic electron fluxes coincided with the appearance of the super-dense electron and ion plasma sheet at synchronous orbit. The dropouts also coincided with the formation of the plasmaspheric drainage plume which favours the development of EMIC waves. Borovsky and Denton (2009) concluded that the observed losses were due to pitch angle scattering by EMIC waves. The statistical study by Turner *et al.* (2019) extended previous statistical studies of the response of radiation belt electrons to geomagnetic storms by investigating solar wind drivers of the geomagnetic storms. Their analyses included a total of 110 storms which occurred between September 2012 and September 2017. Five categories of solar wind drivers identified were (i) CME sheath only, (ii) CME ejecta only, (iii) full CMEs consisting of both sheath and ejecta, (iv) Stream interaction regions (SIRs), and (v) unclear and complex events including those with multiple driver events in the solar wind. They reported that full CMEs are effective drivers of multi-MeV electrons enhancements at L < ~ 5 while SIRs are effective drivers of multi-MeV electrons enhancements at L > ~4.5. They also reported that geomagnetic storms driven by partial CMEs, either CME sheaths or CME ejecta only have the highest probability to cause prolonged depletions of multi-MeV electrons throughout the outer belt. Turner et al. (2019) also provided an excellent summary of previous work characterizing the response of radiation belt electrons to different types of storm drivers.

Although significant progress has been made since the launch of the Van Allen Probes (VAPs) in understanding the response of the radiation belt particles to different solar wind and geomagnetic conditions, not many studies have discussed ionospheric precipitation during these events. Precipitation of energetic particles into the ionosphere causes the absorption of radio signals, thereby disrupting communication between transmitter and receiver. Furthermore, most studies investigating electron flux dropout events have

considered dropouts associated with extreme geomagnetic and/or solar wind conditions such as during CMEs. On most days, solar wind and geomagnetic activity levels are far from extreme. Therefore, an understanding of the mechanisms associated with electron precipitation during quieter conditions, in comparison with elevated geomagnetic activity levels, will facilitate the development of strategies to mitigate their adverse consequences on radio signals. Hence, this study is focused on flux dropout events occurring during moderate solar wind and geomagnetic conditions, and the associated mechanisms of ionospheric precipitation during these events.

Events selection, data, and methodology

The orbital period of the VAPs is ~ 9 hours, therefore a depletion interval in this analysis is considered as one during which the electron flux detected by the VAPs at a particular time is lower than the flux detected in the preceding 9 hours to that time.

Turner *et al.* (2009) considered a total of 280 storms out of which 91 were triggered by CIRs. A superposed epoch analysis (SEA) of Dst index during the CIR storms showed the minimum Dst index as ~ -70 nT. Therefore, a minimum SYM-H index of -80 nT was imposed on all the events included in this study. In addition, only flux depletion events which extended below L = 5 were selected. This was in order to remove depletion events that may have been specifically caused by drift-shell splitting (e.g. Takahashi *et al.*, 1997; Sibeck *et al.*, 1987; Selesnick and Blake, 2002). Since solar wind and geomagnetic conditions are extremely variable over time, wide variations of these conditions may be evident over extended radiation belt electron flux depletion intervals. Therefore, in order to determine the dominant solar wind and geomagnetic conditions associated with a flux depletion event, only events associated with continuous flux dropout of duration $\leq$ 24 hours were considered.

In order to determine the occurrence of electron flux depletion from the radiation belts, fluxes of these electrons spanning October 2012 – December 2018 were visually analysed from L-shell plots available on the Van Allen Probes Science Gateway. Data for the L-shell plots can be selected from a suite of particles and fields measurement instruments on board the VAPs. For this study, level-2 spin-averaged differential electron fluxes from the Relativistic Electron Proton Telescope (REPT) (Baker et al., 2013) of the Energetic particle, Composition, and Thermal plasma (ECT) suite (Spence et al., 2013) was selected. Additional data were obtained from the Magnetic Electron and Ion Spectrometer (MagEIS). In order to avoid counting the same event twice, all the events were selected from one of the Radiation Belt Storm Probes (RBSP) A or B, depending on which probe detected the dropout first. After determining intervals which satisfied the selection criteria outlined in the preceding paragraph, the data were downloaded from the OMNI VAPs (Radiation Belt Storm Probes (RBSP)) database.

For each dropout interval, the geomagnetic conditions (determined by SYM/H and AL-indices) as well as solar wind conditions (flow speed, flow pressure, proton density, azimuthal velocity, and IMF Bz) were determined. Solar wind data, SYM/H and AL indices were obtained from the OMNI dataset and the maximum (positive magnitude) of SYM/H and AL-index for each flux dropout interval were used as indicators for storm or substorm occurrence respectively.

Dst index from the World Data Centre for Geomagnetism, Kyoto were not available, at the time of preparation of the manuscript, for the entire study interval. However, SYM/H indices were available for all the years included in the study, therefore SYM/H index was used as an indicator of the ring current magnitude. Cosmic noise absorption (CNA) derived from the riometer at Sodankyla Geophysical Observatory (SGO) was also examined in order to determine if ionospheric precipitation occurred during selected flux depletion events. The magnitude of flux dropout was calculated by subtracting the flux levels across all L-shells and energy channels during the dropout interval from the corresponding data ~ 9 hours prior to the dropout.

It should be noted that electron fluxes, especially at high energies ($\geq$ 5.2 MeV), can be very low and the ratio of flux levels before dropout to the levels after dropout for this energy range can be rather large compared to the corresponding ratios at lower energy channels which have higher pre- and post dropout flux levels. Moya e*t al.* (2017) reported

Superposed epoch analysis

greater differences between flux levels before and after an enhancement event than corresponding flux levels before and after a depletion event. Claudpierre *et al.* (2015) showed that instrument background noise can swamp actual flux measurements for MeV electrons at very low L-shells and at large L-shells when the flux is ≤ 10 cm-2 s-1 sr-1 MeV-1. Therefore, as a further precaution to eliminate 'false' depletion events, flux levels below 50 cm-2 s-1 sr-1 MeV-1 were removed from the analysis. This noise threshold is similar to that used by Moya *et al.* (2017). Therefore, in this work an event was recorded as depletion if the difference between the pre- and post-depletion levels of electron flux was ≥ 50 cm-2 s-1 sr-1 MeV-1. The energy levels and corresponding L-shells which did not satisfy the above conditions were blanked out in the L-shell vs. energy plots (e.g. Figure 1).

A superposed epoch analysis (SEA) of the aforementioned geomagnetic indices and solar wind parameters was also undertaken. All of the selected events were associated with substorm (AL-index ≤ -300 nT), therefore epoch 0 is the time of maximum dip in AL-index corresponding to the commencement of flux dropouts. Based on the event selection criteria, the epoch analysis interval includes 9 hours before, and 24 hours after epoch 0. Finally, phase space density (PSD) profiles from Van Allen Probes Science Gateway were analysed to determine the adiabatic effect in the observed flux depletions. A total of 46 clear dropout events spanning September 2012 to December 2018, which extended below L=5, and lasted for ≤ 24 hours were recorded. Of the 46 events, 27 were associated with CIR storms and 9 were associated with CME storms. The remaining events did not exhibit clear (or exclusive) CIR or CME storm characteristics. The CIR storms were further separated into those without a SSC signature but with SYM/H index ≥ -80 nT (moderate CIR storms), and those with SYM/H ≤ - 80 nT and/or accompanied by a SSC signature (large CIR storms).

Results

The flux dropout events associated with moderate CIR storms showed a distinct association with substorm expansion phase and recovery; hence, the results presented in this paper pertain to the moderate CIR events. A list of all the moderate CIR storms included in the study is provided in Table 1. The averaged magnitude of flux depletion as a function of L-shell and energy for the dropout events associated with moderate CIR storms (a total of 16 events) is shown in Figure 1. The largest depletion magnitudes were recorded for 1.8 MeV electrons at 4.6 ≤ L ≤ 4.9. The results from a SEA of the 16 moderate CIR associated events, with epoch 0 as the time of maximum dip in AL-index corresponding to the commencement of flux dropouts, are shown in Figures 2 and 3. The mean, median, upper and lower quartiles of the solar wind parameters and geomagnetic activity indices are shown as the brown, purple, blue and green lines respectively in Figure 2. Figure 3 shows the variation of averaged fluxes, binned by energy, with L-shell and epoch time.

Table 1: List of all the moderate CIR storms included in the study, according to year.

2013	**2016**	**2017**	**2018**
4 August	1 May	18 January	5 July
27 August	5 June 2016	1 March	10 September
	2/3 August	19 April	21/22 September
	29/30 August	17 August	7 October
		27 September	4 November

Superposed epoch analysis

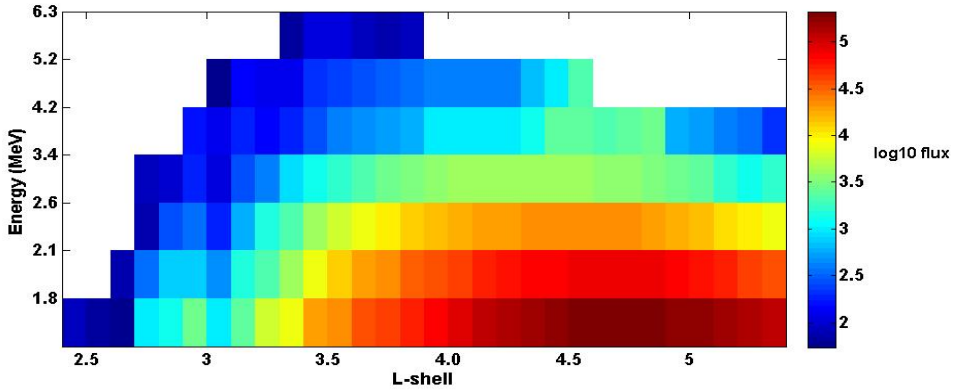

Figure 1: Averaged flux depletion as a function of L-shell and energy of 16 CIR associated flux depletion events

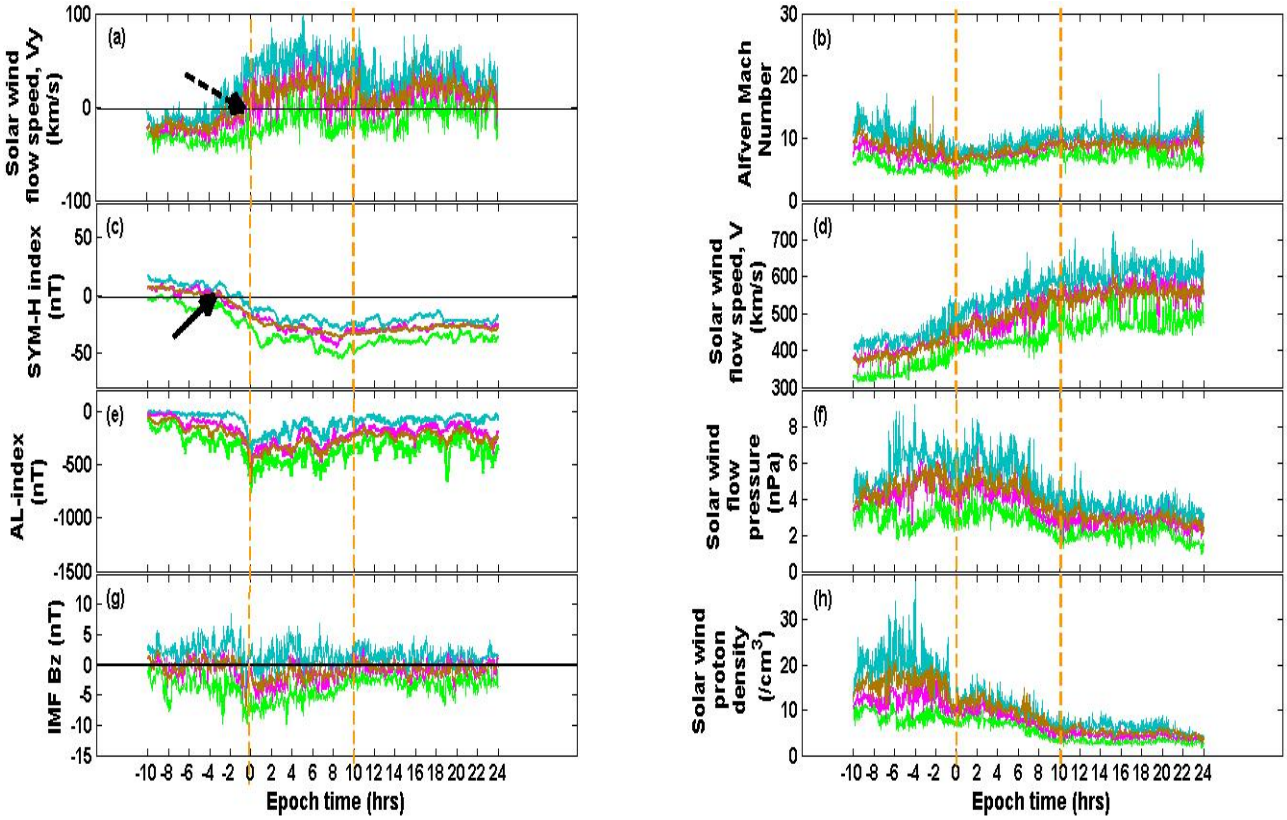

Figure 2: Superposed epoch analysis of solar wind parameters and geomagnetic activity indices. (a) Azimuthal component of solar wind speed (b) Alfven mach number (c) SYM-H index (d) Solar wind speed (e) AL-index (f) Solar wind flow pressure (g) z-component of the solar wind magnetic field (h) Solar wind proton density. The superposition of 16 CIR associated flux depletion events is shown. Epoch 0 is the time of maximum dip in AL-index corresponding to the commencement of flux dropout. The brown, purple, blue and green lines represent the mean, median, upper quartile and lower quartile respectively of each dataset. Black solid and dotted arrows indicate storm onset and HSS passage, respectively.

Superposed epoch analysis

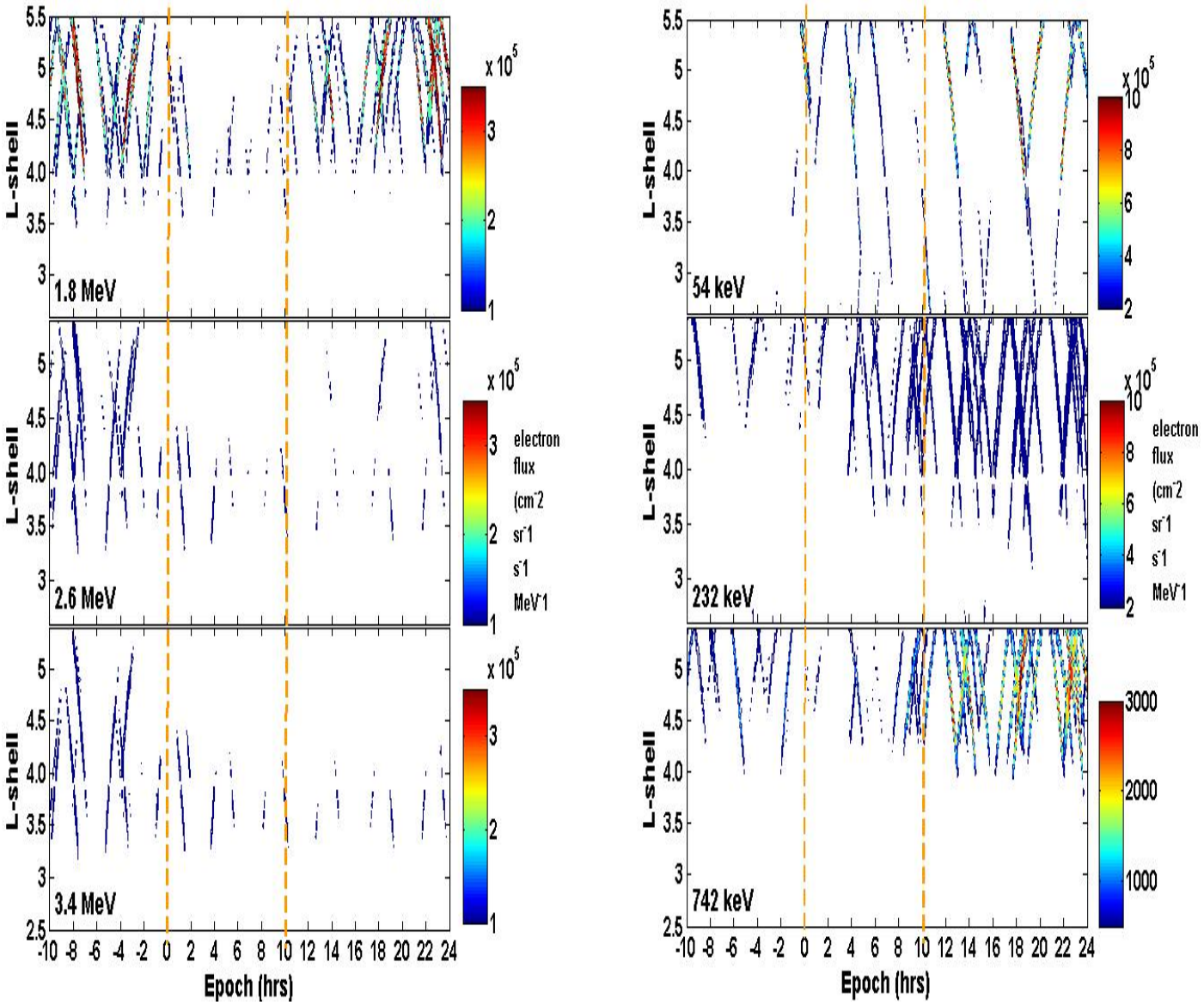

Figure 3: Superposed epoch analysis of radiation belt fluxes for keV and MeV electrons. The superposition of 16 CIR associated flux depletion events is shown. The flux levels of the MeV electrons (left panel) are similar; hence, the scales on the colourbar for these electrons are same. However, on the right panel, fluxes of 54 keV electrons are much higher than for any other population while the flux levels of the 742 keV population is least of all.

The hallmarks of a CIR driven storm (Borovsky and Denton, 2006) are evident in the parameters displayed in Figure 2. For example, the azimuthal component of the solar wind flow speed, V_y , in Figure 2a shows the characteristic reversal in direction from westward to eastward. In Figure 2c SYM/H index decreased gradually to minimum values ($\geq$ -80 nT), signifying moderate storms. In addition, the storm sudden commencement (SSC) signature, more typical of CME storms, was not prominent. Fluctuations in IMF Bz typical of CIR storms are also evident in Figure 2g. The gradual rise in solar wind flow speed, accompanied by high solar wind flow pressure and proton density appearing ahead of the fast solar wind stream, typical of CIR storms is evident in Figures 2d, 2f and 2h. The Alfven

Superposed epoch analysis

Mach number also shows evidence of shocks before the passage of the HSS. Closer examination of SYM/H and V_y in Figures 2c and 2a respectively shows that the storm onset (indicated by solid arrow) occurred ~ 2 hours before the HSS passage (indicated by dotted arrow), similar to Figure 3 in Borovsky and Denton (2009).

The dropout of 1.1 – 1.5 MeV radiation belt electron fluxes during 124 HSS driven storms were investigated by Borovsky and Denton (2009). They further sub-classified the events according to those which exhibited clear onsets of flux dropouts, those that exhibited rapid recoveries of fluxes, and those for which the fluxes were not significantly affected by the storms i.e. no clear onset of dropouts or recovery of fluxes. All of the events included in this study showed clear onset and recovery, especially in the 1.8 MeV band, similar to the 1.1 – 1.5 MeV band considered by Borovsky and Denton (2009). In Figure 2c and Figure 3, it is obvious that maximum flux dropout of 1.8 MeV electron fluxes occurred during main phase of storm. This result is similar to the SEA by Borovsky and Denton (2006), of 33 events which exhibited clear onsets of flux dropouts. Another similarity with the SEA by Borovsky and Denton (2006) is the coincidence of dropout onset with southward IMF Bz (Figure 2g and Figure 3 (1.8 MeV)). The results of Borovsky and Denton (2006) showed that passage of the HSS occurred several hours after IMF Bz turned southward (6 - 16 hours). However, the SEA in Figure 2 shows that the passage of the HSS coincided with southward turning of IMF Bz. A factor that may account for this observed difference is the selection criteria. Borovsky and Denton (2006) selected only storms that were preceded by and/or followed by another storm 27 days earlier or later. However, this criterion was not enforced in selection of events included in this paper.

Figure 3 shows the superposed epoch analysis of the different radiation belt electrons populations to the 16 moderate CIR storms.

Superposed epoch analysis

The response of the 1.8 MeV population appears to be adiabatic with the flux levels returning to pre-storm levels ~ 10 hours after epoch 0. The timings of onset of flux dropout and flux recovery of the 1.8 MeV population most closely match epoch 0 time (minimum AL-index during substorm main phase) and substorm recovery respectively. Fluxes of > 1.8 MeV electrons started to undergo dropout at higher L-shells before epoch 0, ~ 2 hours before the passage of the stream interface. In addition, the recovery time of fluxes of > 1.8 MeV electrons increased with increasing energy. However, beginning from epoch 0, fluxes of 54 keV electrons experienced enhancement across all L-shells as the storm progressed. The population of 232 keV electrons also increased progressively as the storm progressed, although flux levels were significantly less than for 54 keV electrons. However, the 742 keV population appeared to be driven by competing loss and acceleration mechanisms during the highlighted 10-hour epoch interval. Beyond epoch 10 hours, the enhancement of fluxes of this population of electrons is evident. Furthermore, the fluxes of this population were by far the lowest in the entire population studied. The blank regions in the orbits indicate that the fluxes in these regions were below the threshold applied to the data. The statistical results of Turner *et al.* (2019) also showed enhancement of 55 keV, 237 keV and 897 keV electrons fluxes during CIR driven storms. The response of the 54 keV and 232 keV and 742 keV electron fluxes in Figure 3 are in agreement with the results of Turner e*t al.* 2019.

Three different events were selected for further analysis in order to investigate the possible mechanisms associated with the observed flux dropouts and whether or not ionospheric precipitation occurred during these events. The events were selected from the upper quartile, lower quartile, and mean distributions of SYM/H index in Figure 2c. The Comprehensive Inner Magnetosphere-Ionosphere (CIMI) model, hosted by the

Community Coordinated Modeling Center (CCMC), was run with different input parameters to gain insight into possible mechanisms associated with the observed radiation belt losses. The CIMI model (Fok et al., 2011, 2014) is a kinetic model that simulates the response of radiation belt and ring current species under various solar wind and magnetic conditions. The model combines the Comprehensive Ring Current Model (CRCM) (Fok et al. 2001b, 2005) and Radiation Belt Environment (RBE) model (Fok *et al*., 2001a, 2005, 2008, 2011; Zheng e*t al*., 2003; Glocer *et al*., 2009), thereby incorporating a self-consistent electric field and accurate wave-particle interactions to describe the behaviour of these species. Of the three selected events, model results most closely matched the experimental observations of the event selected from the upper quartile. This event, which occurred 5 June 2016, is henceforth referred to as Event 1. Hence, the model results and discussion section are focused mainly on Event 1.

CIMI Model Results for Event 1: 5 June 2016 (Above Upper Quartile)

The solar wind conditions during the 3 selected events are shown in Figure 4. In Figure 4a, SYM/H for Event 1 lies above the upper quartile distribution in the epoch interval. Solar wind proton density was highest during this event and passage of the HSS occurred last for this event. The first CIMI model run for Event 1 was executed with the Tsyganenko-Sitnov 2004 magnetic field model, Weimer-2000 ionosphere electric field model, OMNI solar wind parameters, and lower band chorus wave as the loss mechanism. These results will be referred to as Run 1 in the rest of this paper. The model results for all selected events are on publication at the Community Coordinated Modeling Center (CCMC). Information on selected CIMI wave loss mechanisms and CCMC registration numbers for Event 1 is provided in Table 2. Model outputs (plasmasphere pressure and density, flux distributions of 1.78 MeV and 3.16 MeV electrons) for Event 1 showed two key features of interest. The first is the appearance of oscillations on the dayside magnetosphere boundary, similar to surface waves generated by the Kelvin Helmholtz instability (KHI), and which are known to be associated with ultra-low frequency (ULF) waves (Agapitov and Cheremnykh, 2013). The second model result of interest is that the greatest depletion of fluxes occurred on the nightside.

In order to visualize plasmasphere density and the distribution of fluxes in the absence of any simulated wave loss mechanism, the model was run with the same input parameters but with no wave loss mechanism selected i.e. neither lower band chorus waves nor hiss waves were selected (Run 2). The fluxes of source and seed populations of electrons from Run 1 were slightly higher than from the second model run (Run 2). However, there was no change in the fluxes of $>$ 1 MeV electrons from Run 1 compared with Run 2. The important result to note here is that the chorus waves had no contribution to the depletions of > 1 MeV electron fluxes. Model results with plasmaspheric hiss only as loss mechanism (Run 3) showed noticeable depletion of fluxes only for 1.78 MeV electrons and this occurred in the slot region ($2.5 < L < 4.0$). Outside this region, no clear effect was evident. Model results from Runs 1, 2 and 3 showed that lower band chorus waves and plasmaspheric hiss had little or no contribution to the observed flux depletions of $>$ 1 MeV electrons at $L > 4.0$.

Superposed epoch analysis

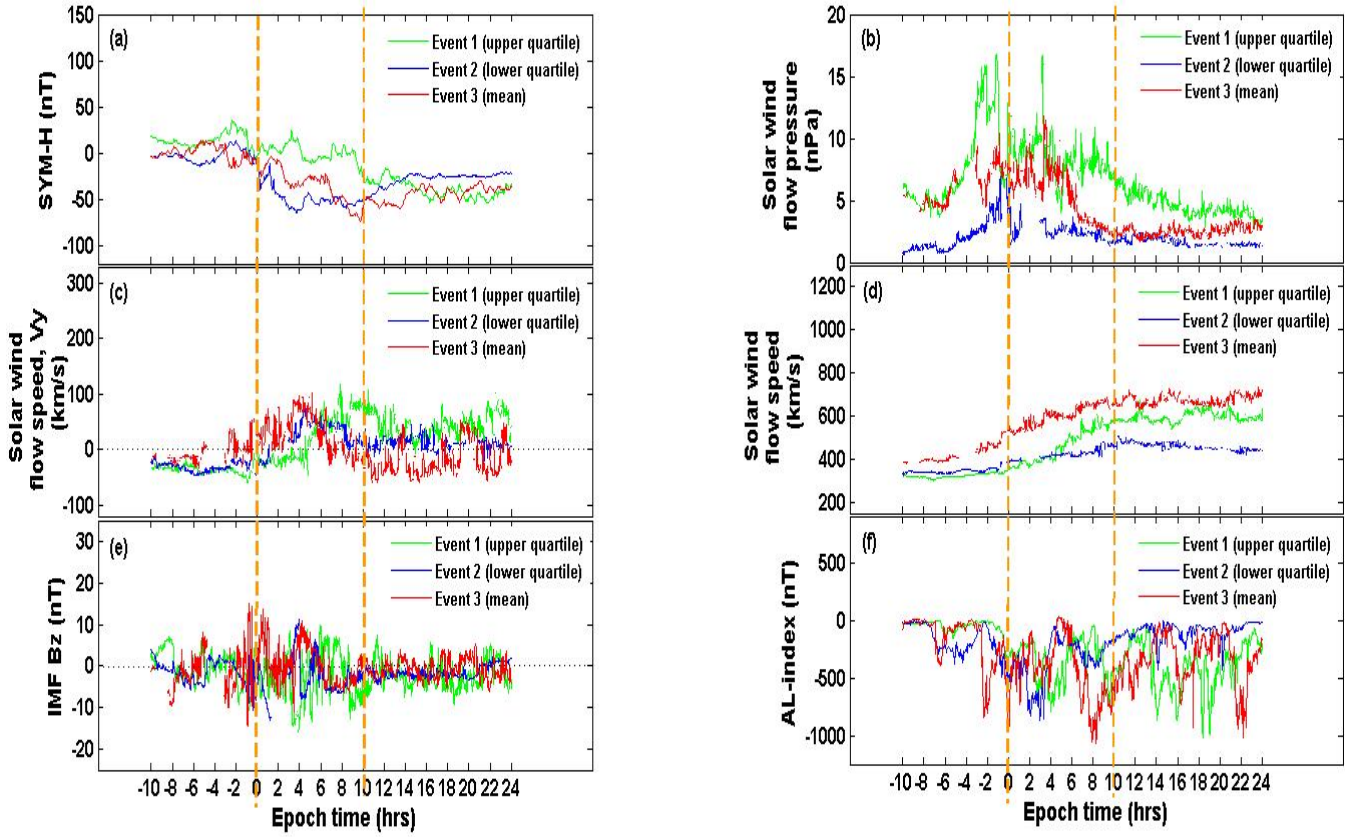

Figure 4: Superposed epoch analysis of solar wind parameters and geomagnetic activity indices. (a) SYM-H index (b) Solar wind flow pressure (c) Azimuthal component of solar wind speed (d) Solar wind speed (e) z-component of the solar wind magnetic field (f) AL-index. The superposition of 3 selected events is shown.

Table 2: Wave loss mechanisms selected in CIMI model for each of the 3 modeled events and the corresponding CCMC registration numbers for each model run.

Event	Run number	Modeled wave loss mechanism	CCMC Registration number
Event 1	1	Lower band chorus only	Busola_Olugbon_061319_IM_1
	2	None	Busola_Olugbon_061419_IM_1
	3	Hiss only	Busola_Olugbon_062019_IM_1

Discussion

Borovsky and Denton (2009) showed that the dropout of relativistic electron fluxes coincided with the appearance of super-dense electron and ion plasma sheet at synchronous orbit. The dropouts also coincided with appearance of the plasmaspheric drainage plume which facilitates growth of EMIC waves. Although data from the multi-spacecraft Magnetospheric Plasma Analyzer (MPA) were unavailable during Event 1, modeling of the Earth's inner magnetosphere showed that there was no appearance of super-dense plasma sheet or plasmaspheric plume. During Event 1, magnetic Waveform Receiver (WFR) data from the VAPs (Kletzing et al. 2013) and the magnetic footprint of the VAPs showed that chorus waves on 5 June 2016 were most intense when the probes were located on the dawn flank at 1400 – 2000 UT. Combined results from data analysis and modeling suggest

Superposed epoch analysis

that 54 keV electrons were injected during substorm and generated chorus waves on the dawn flank. These waves can accelerate seed population to relativistic speeds via gyro-resonant interactions, thereby replenishing the core population. This is in line with current understanding that source population of radiation belt electrons facilitates generation of chorus waves, which interact with a seed population thereby accelerating them to relativistic energies (Turner et al., 2015).

The CIMI fluxes of 1.78 MeV electrons during Event 1 showed that the greatest depletion of fluxes of this population occurred on the nightside. In order to determine if ionospheric precipitation occurred during this event, cosmic noise absorption (CNA) derived from the riometers at Sodankyla Geophysical Observatory (SGO) was examined. Figure 5a - e show CNA on 5 June 2016 from 5 observatories located on closely spaced meridians and arranged in decreasing order of latitude from top-to-bottom. Figure 5f and 5g are the X-component geomagnetic field data from ground magnetometer stations PEL and TIK (Tanskanen, 2009; Gjerloev 2012). PEL is nearly co-located with the riometer at ROV but TIK is separated in local time from the riometer stations. The coordinates of the riometer and magnetometer locations are given in Table 3. Local time at the riometer stations and at the ground magnetometer station PEL is ~ UT + 3, while local time at the ground magnetometer station (TIK) is ~ UT + 9. Absorption was significant in CNA computed from riometer data at IVA, SOD, and ROV from ~ 1800 – 2100 UT. It is not surprising that CNA was most significant at the auroral latitudes, as the configuration of geomagnetic field lines at these latitudes facilitates the transportation of particles from space to the Earth's atmosphere. Similarly, ULF pulsations in the geomagnetic field data from PEL were largest at this time. It should be noted that large amplitude oscillations in the ULF band appeared much earlier in the geomagnetic field data from TIK (~1300 - 2300 UT). Interestingly, the ground geomagnetic pulsations at TIK appeared only when the local time of the ground station crossed into nighttime. Figure 6 shows the time series of data from TIK, PEL, and ROV during local nighttime at each station. A fast Fourier transform (FFT) of the time series during these intervals showed a dominant ~ 1.0 mHz oscillation in the data.

Table 3: Geomagnetic coordinates of riometer and magnetometer locations from which data were analyzed

Station name	**Station code**	**Geomagnetic longitude**	**Geomagnetic latitude**
		Riometer Stations	
Abisko	ABI	101.82°	65.18°
Ivalo	IVA	108.61°	65.03°
Sodankyla	SOD	107.29°	63.81°
Rovaniemi	ROV	104.95°	63.42°
Oulu	OUL	105.33°	61.47°
Jyvaskyla	JYV	104.63°	58.51°
		Magnetometer Stations	
Pello	PEL	104.95°	63.42°
Tixie	TIK	-162.65°	66.04°

Superposed epoch analysis

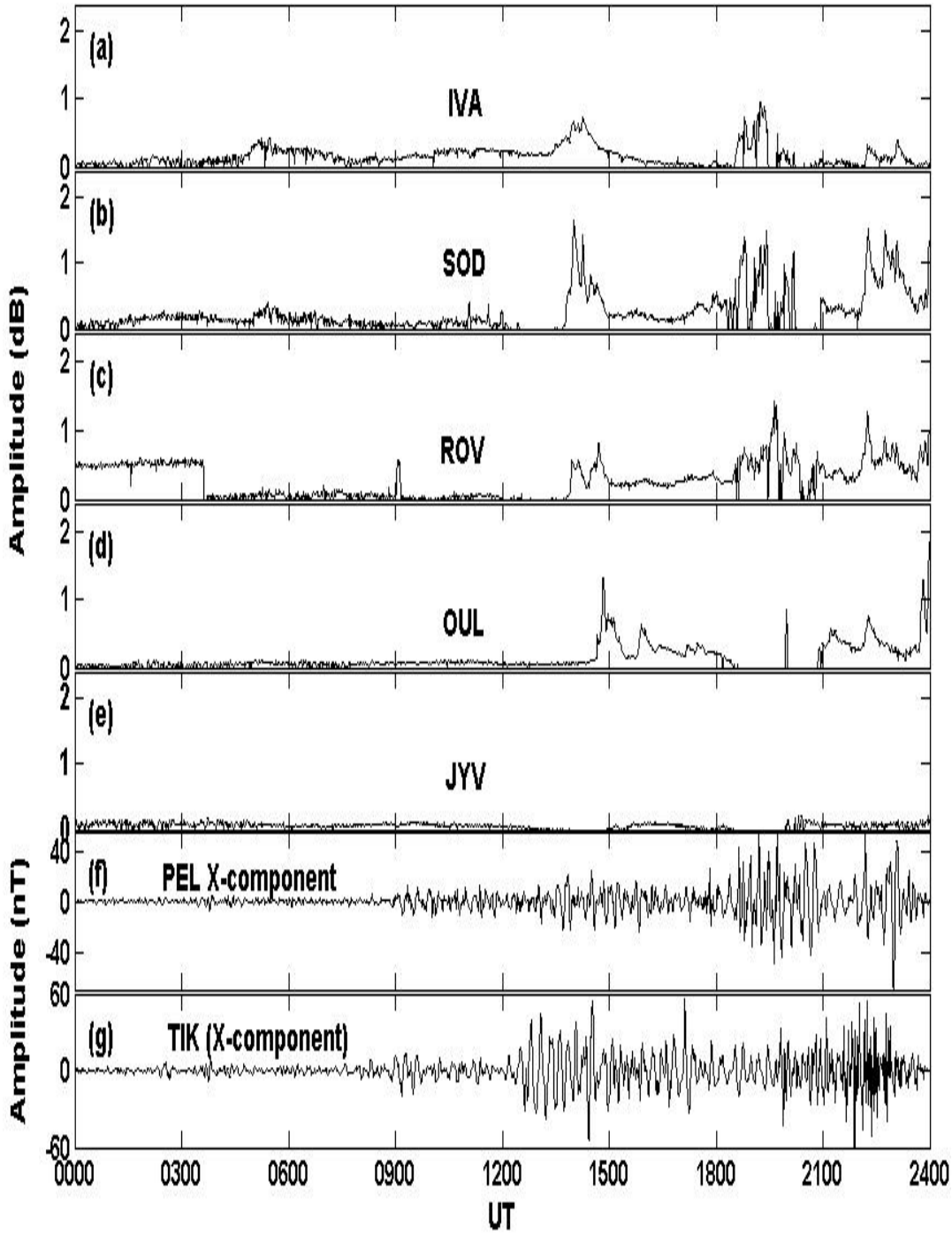

Figure 5: a – e) Cosmic noise absorption (CNA) derived from the riometer data at Sodankyla Geophysical Observatory f – g) X-component geomagnetic field data from PEL and TIK. CNA is evident from 5 observatories located on closely spaced meridians but separated in latitude. Large amplitude oscillations are evident at ~ 1400 – 1500 UT and 1900 – 2400 UT in CNA. Oscillations in geomagnetic field data start ~ 1300 UT (TIK), ~ 1900 UT (PEL) and continue till ~ 2300 UT.

Superposed epoch analysis

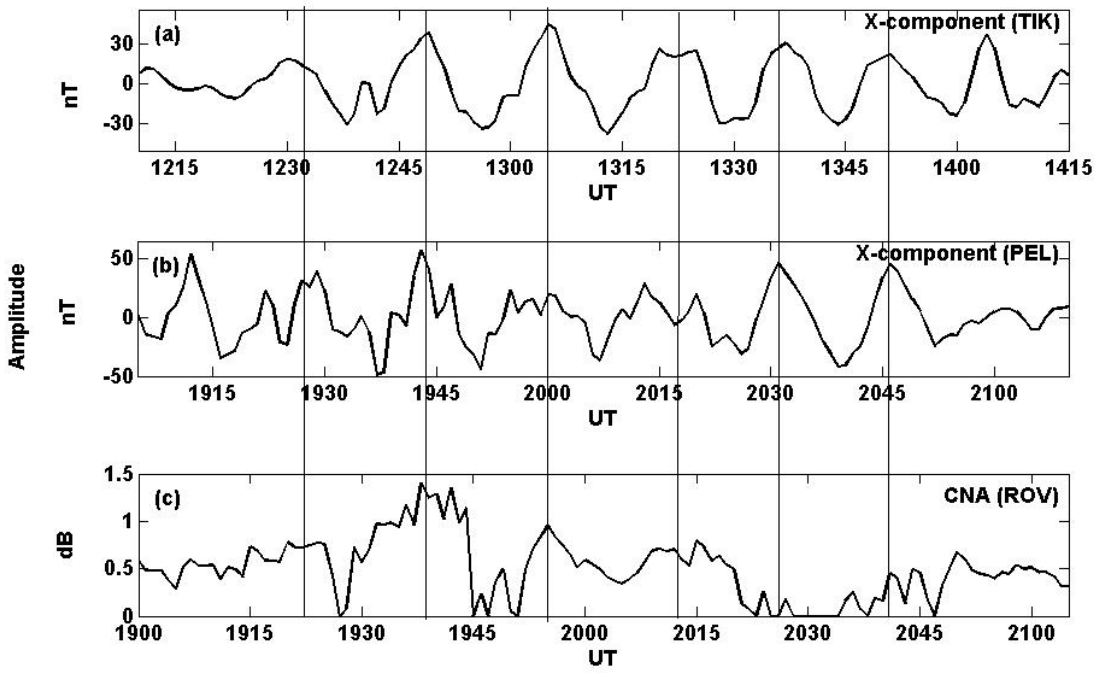

Figure 6: Time series of X-component geomagnetic field data from a) TIK and b) PEL c) cosmic noise absorption from ROV, 5 June 2016. The local time at TIK is UT+9 while at ROV, the local time is UT+3. Similar oscillations in the ULF band are present in the data sets.

These results strongly suggest that the dominant dropout mechanism was localized to the midnight sector and the hours flanking midnight. Since the depletions were more pronounced at nighttime, it is unlikely that magnetopause shadowing would have caused the losses. Similarly, lobe encounters are unlikely because these encounters are known to occur for short durations, typically in the range of minutes and are predominant at or near geosynchronous orbit (Soto-Chavez *et al.*, 2016). Only data from $L \leq 5.5$ were included in the analysis in this paper. Borovsky and Denton (2009) noted that fluxes of 1.1 – 1.5 Mev electrons were most depleted in the region where plasmasphere density was densest, and EMIC waves most predominant. For Event 1, results show that flux dropout was greatest in the region where large amplitude ULF waves were localized. The results from modeling showed that plasmasphere density was not super dense during any of the selected events. Plasmaspheric hiss was observed in the magnetic WFR data from the VAPs for most of the day. However, modeling showed that the contribution to flux dropout from these waves was rather small to account for the observed losses during this event.

The radial profiles of phase space density (PSD) for this event are shown in Figure 7. Inbound 1 pass in Figure 7 refers to the passage of RBSP-A before the dropout was observed. Inbound passes 2 and 3 occurred during the observed dropout, while inbound pass 4 occurred post-dropout. The PSD was computed for selected electron energies between 900 MeV/G (corresponding to ~ 1.09 MeV at L*=5.0) and 1500 MeV/G (corresponding to ~ 1.51 MeV at L* = 5.0). The transition of the PSD profiles (Figure 7a – 7e) from inbound pass 2 to inbound pass 3 closely resembles that associated with outward radial transport as illustrated in Figure 1.4 of Turner and Ukhorskiy (2020). The peak in the PSD during the inbound pass 2 is seen to decrease and move to a lower L-shell during inbound pass 3.

Superposed epoch analysis

This is not surprising since ULF waves, which are known to drive outward radial transport, were evident during this event. The region 4.9 < L* < 5.4 in Figure 7e was highlighted to emphasize the decrease in PSD in inbound pass 2 relative inbound pass 1. This occurred for electrons of μ=1100 MeV/G, corresponding to ~ 1.3 MeV at L* = 5.4 and with equatorial pitch angles ~ 41°. This L* interval is in the vicinity of the L-shell values of the riometer and magnetometer locations in Table 1. In Figure 7f, it appears that the localized losses also affected higher energy electrons. This suggests that losses due to ULF wave activity are pitch angle and energy dependent. However, outward radial transport appears to be independent of electron energy or pitch angle. The PSD profiles also show that these losses were not adiabatic. Likewise, data from the RBSP ECT-REPT for this event showed that electron fluxes with energy ≥ 1.8 MeV did not recover adiabatically.

Although ULF waves have been reported to occur simultaneously with flux dropout and precipitation of radiation belt electrons to the atmosphere, they have not been established to be directly responsible for the precipitation events. However, it is generally accepted that ULF waves could modulate EMIC wave growth rates which cause loss of energetic particle fluxes via pitch angle scattering into the atmospheric loss cone. Rae et al. (2018) presented experimental evidence of precipitating electron fluxes modulated by ULF waves and concluded that compressional ULF waves should be considered a direct, rather than an indirect, precipitation mechanism for radiation belt electrons. Experimental observations from this study show a clear association of ionospheric precipitation of radiation belt electrons with ULF waves. However, further work will be required to establish the actual mechanisms for the observed radiation belt flux depletions. In previous studies, wave structures have been linked with the occurrence of ionospheric irregularities at equatorial latitudes (Olugbon *et al.*, 2021, 2022, 2024). These findings further highlight the role of wave structures in ionospheric electrodynamics, both at equatorial and higher latitudes.

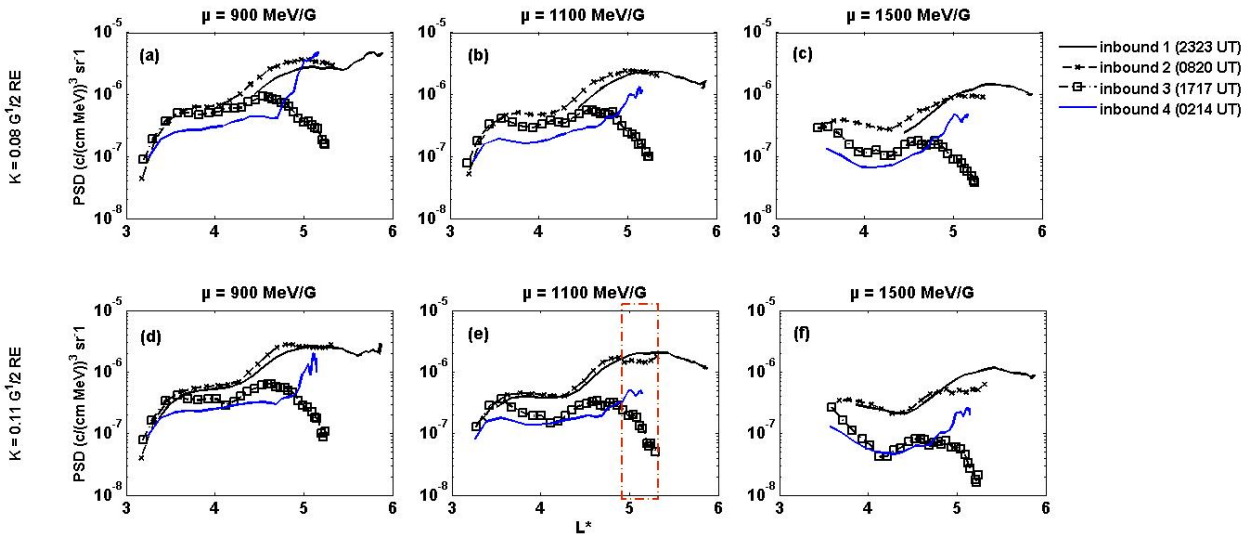

Figure 7: Phase space density (PSD) profiles during the flux dropout event 5 June 2016. The PSD profiles were computed for constant μ. (a, d) μ=900 MeV, (b, e) μ=1100 MeV, and (c, f) μ=1500 MeV, and constant K. (a – c) K=0.08 G1/2 RE and (d – f) K=0.11 G1/2 RE. Note that Inbound pass 1 occurred 4 June 2016, while inbound pass 4 occurred 6 June 2016. The boxed area in panel (e) shows a decrease in PSD associated with ultra-low frequency wave activity.

Superposed epoch analysis

Summary and Conclusions

This study investigated the dropout of radiation belt electrons fluxes during moderate CIR driven storms. Statistical findings showed that the dropouts were energy dependent with depleted 1.8 MeV electrons returning to pre-depletion levels after the storm and true losses occurring for fluxes of higher energy electrons. The greatest dropouts occurred for 1.8 MeV electrons at $4.6 \leq L \leq 4.9$. Although the 1.8 MeV electron fluxes returned to pre-depletion levels after the storm, phase space density measurements showed that the 1.8 MeV electron flux losses were not adiabatic. Results from the Comprehensive Inner Magnetosphere-Ionosphere (CIMI) model closely matched observed results from an event which was selected from the upper quartile of a superposed epoch analysis. The model results showed surface waves on the dayside magnetopause, similar to waves generated by the Kelvin Helmholtz instability. These types of surface waves have been associated with ULF waves in previous studies. Model results for the selected event also showed that the greatest losses occurred on the nightside. Analysis of data from the Van Allen probes showed that the nighttime losses extended to lower L-shells and affected fluxes of higher MeV electrons compared with dayside losses. Cosmic noise absorption measurements also showed significant nighttime absorption for the selected event. The results from this study further highlight the possible role of ULF waves in the dropout of radiation belt electrons fluxes. The results presented also demonstrate the capability of the CIMI model in reproducing real events. It should be noted that the events were simulated with version 20170426 of the model since it was the latest available version at the time of preparation of the manuscript. However, newer versions are currently available and it will be interesting to investigate how the newer versions perform in comparison with older versions.

Superposed epoch analysis

Acknowledgements

The authors acknowledge the NASA Van Allen Probes and Craig Kletzing (University of Iowa) for use of data. Processing and analysis of the MagEIS and REPT data was supported by Energetic Particle, Composition, and Thermal Plasma (RBSP-ECT) investigation funded under NASA's Prime contract no. NAS5-01072. All RBSP-ECT data are publicly available at the Web site http://www.RBSP-ect.lanl.gov/. The authors acknowledge Dan Baker for providing the REPT data, Harlan Spence (PI) and Geoff Reeves (Science Team Lead) for providing the ECT data. Simulation results have been provided by the Community Coordinated Modeling Center at Goddard Space Flight Center through their public Runs on Request system (http://ccmc.gsfc.nasa.gov). The Comprehensive Inner Magnetosphere-Ionosphere (CIMI) model was developed by Mei-Ching H. Fok and Natalia Buzulukova at the Community Coordinated Modeling Centre (CCMC), NASA GSFC. The authors are grateful to J. H. King and N. Papatashvilli and NASA CDAWeb team for the OMNI solar wind data. The authors gratefully acknowledge E.I. Tanskanen for the geomagnetic field data, which are publicly available at SuperMAG (http://supermag.jhuapl.edu/mag/). CNA was derived from the riometer at Sodankyla Geophysical Observatory (SGO). The authors gratefully acknowledge T. Raita for making CNA data available.

References

Agapitov, O. V. and Cheremnykh, O. K.(2013) Magnetospheric ULF waves driven by external sources. *Advances in Astronomy and Space Physics* 3, 12–19

Baker, D., Kanekal, S., Hoxie, V., Batiste, S., Bolton, M., Li, X., ... and Westfall, J. (2013). The Relativistic Electron-Proton Telescope (REPT) Instrument on Board the Radiation Belt Storm Probes (RBSP) Spacecraft: Characterization of Earth's Radiation Belt High-Energy Particle

Populations. *Space Science Reviews*, 179. doi:10.1007/s11214-012-9950-9

Borovsky, J. E., and Denton, M. H. (2006). Differences between CME-driven storms and CIR-driven storms. *Journal of Geophysical Research: Space Physics,* 111(A7). doi.org/10.1029/2005JA011447

Borovsky, J. E., and Denton, M. H. (2009). Relativistic-electron dropouts and recovery: A superposed epoch study of the magnetosphere and the solar wind. *Journal of Geophysical Research: Space Physics,* 114(A2). doi.org/10.1029/2008JA013128

Bortnik, J., Thorne, R. M., O'Brien, T. P., Green, J. C., Strangeway, R. J., Shprits, Y. Y., and Baker, D. N. (2006). Observation of two distinct, rapid loss mechanisms during the 20 November 2003 radiation belt dropout event. *Journal of Geophysical Research: Space Physics,* 111(A12). doi.org/10.1029/2006JA011802

Claudepierre, S. G., O'Brien, T. P., Blake, J. B., Fennell, J. F., Roeder, J. L., Clemmons, J. H., ... and Reeves, G. D. (2015). A background correction algorithm for Van Allen Probes MagEIS electron flux measurements. *Journal of Geophysical Research: Space Physics,* 120(7), 5703-5727. doi:10.1002/2015JA021171

Fok, M. C., Buzulukova, N. Y., Chen, S. H., Glocer, A., Nagai, T., Valek, P., and Perez, J. D. (2014). The comprehensive inner magnetosphere-ionosphere model. *Journal of Geophysical Research: Space Physics,* 119(9), 7522-7540. doi:10.1002/2014JA020239

Fok, M. C., Ebihara, Y., Moore, T. E., Ober, D. M., and Keller, K. A. (2005). Geospace Storm Processes Coupling the Ring Current, Radiation Belt and Plasmasphere. Washington DC American Geophysical Union Geophysical Monograph Series, 159, 207.

Fok, M. C., Glocer, A., Zheng, Q., Horne, R. B., Meredith, N. P., Albert, J. M., and Nagai, T. (2011). Recent developments in the radiation belt environment model. *Journal of Atmospheric and Solar-Terrestrial Physics,* 73(11-12), 1435-1443.

Fok, M. C., Horne, R. B., Meredith, N. P., and Glauert, S. A. (2008). Radiation Belt Environment model: Application to space weather nowcasting. *Journal of Geophysical Research: Space Physics,* 113(A3). doi:10.1029/2007JA012558

Fok, M. C., Moore, T. E., and Spjeldvik, W. N. (2001a). Rapid enhancement of radiation belt electron fluxes due to substorm dipolarization of the geomagnetic field. *Journal of Geophysical Research: Space Physics*, 106(A3), 3873-3881. doi:10.1029/2000JA000150

Fok, M. C., Wolf, R. A., Spiro, R. W., and Moore, T. E. (2001b). Comprehensive computational model of Earth's ring current. *Journal of Geophysical Research: Space Physics*, 106(A5), 8417-8424. doi:10.1029/2000JA000235

Gjerloev, J. W. (2012). The SuperMAG data processing technique. *Journal of Geophysical Research: Space Physics,* 117(A9). doi:10.1029/2012JA017683

Glocer, A., Toth, G., Fok, M., Gombosi, T., and Liemohn, M. (2009). Integration of the radiation belt environment model into the space weather modeling framework. *Journal of Atmospheric and Solar-Terrestrial Physics,* 71(16), 1653-1663. doi:10.1016/j.jastp.2009.01.003

Katsavrias, C., Daglis, I. A., and Li, W. (2019). On the statistics of acceleration and loss of relativistic electrons in the outer radiation belt: a superposed epoch analysis. *Journal of Geophysical Research: Space Physics,* 124(4), 2755-2768. doi.org/10.1029/2019JA026569

Kletzing, C. A., Kurth, W. S., Acuna, M., MacDowall, R. J., Torbert, R. B., Averkamp, T., ... and Crawford, D. (2013). The electric and magnetic field instrument suite and integrated science (EMFISIS) on RBSP. *Space Science*

Reviews, 179(1-4), 127-181. doi.org/10.1007/s11214-013-9993-6

Mauk, B. H., Fox, N. J., Kanekal, S. G., Kessel, R. L., Sibeck, D. G., and Ukhorskiy, A. (2013). Science Objectives and Rationale for the Radiation Belt Storm Probes Mission. *Space Science Reviews*, 179, 3-27.

Moya, P. S., Pinto, V. A., Sibeck, D. G., Kanekal, S. G., and Baker, D. N. (2017). On the effect of geomagnetic storms on relativistic electrons in the outer radiation belt: Van Allen Probes observations. *Journal of Geophysical Research: Space Physics*, 122(11), 11-100. doi.org/10.1002/2017JA024735

Olugbon, B., Oyeyemi, E. O., Kascheyev, A, Rabiu, A. B., Obafaye, A. A., Odeyemi, O. O., Adewale, A. O. (2021). Daytime equatorial spread F-like irregularities detected by HF Doppler receiver and digisonde. *Space Weather*, 19(4), e2020SW002676. https://doi.org/10.1029/2020SW002676

Olugbon, B., Oyeyemi, E. O., Kashcheyev, A. (2022). Case Studies on the Day-to-Day Variability in the Occurrence of Post-Sunset Equatorial Spread F. *Space Weather,* 20(9), e2021SW002996. https://doi.org/10.1029/2021SW002996

Olugbon, B., Oyeyemi, E. O., Kashcheyev, A, Rabiu, A. B., and Obafaye, A. A. (2024). Ionospheric signatures from 2 years continuous monitoring of the equatorial ionosphere over Nigeria with HF Doppler sounder. *Advances in Space Research*, 74(11), 6031-6046. https://doi.org/10.1016/j.asr.2024.08.032

Rae, I. J., Murphy, K. R., Watt, C. E., Halford, A. J., Mann, I. R., Ozeke, L. G., ... and Forsyth, C. (2018). The role of localized compressional ultra-low frequency waves in energetic electron precipitation. *Journal of Geophysical Research: Space Physics*, 123(3), 1900-1914. doi.org/10.1002/2017JA024674

Superposed epoch analysis

Reeves, G. D., McAdams, K. L., Friedel, R. H. W., and O'Brien, T. P. (2003). Acceleration and loss of relativistic electrons during geomagnetic storms. *Geophysical Research Letters,* 30(10). doi:10.1029/2002GL016513

Selesnick, R. S., and Blake, J. B. (2002). Relativistic electron drift shell splitting. *Journal of Geophysical Research: Space Physics*, 107(A9), SMP-27. doi:10.1029/2001JA009179

Sibeck, D. G., McEntire, R. W., Lui, A. T. Y., Lopez, R. E., and Krimigis, S. M. (1987). Magnetic field drift shell splitting: Cause of unusual dayside particle pitch angle distributions during storms and substorms. *Journal of Geophysical Research: Space Physics*, 92(A12), 13485-13497. doi.org/10.1029/JA092iA12p13485

Soto-Chavez, A. R., Lanzerotti, L. J., Gerrard, A., Kim, H., Bortnik, J., and Manweiler, J. W. (2016). RBSPICE measurement of ion loss during the 2015 March storm: Adiabatic response to the geomagnetic field change. *Journal of Geophysical Research: Space Physics*, 121(10), 9547-9559. doi:10.1002/2016JA022512

Spence, H. E., Reeves, G. D., Baker, D. N., Blake, J. B., Bolton, M., Bourdarie, S., ... and Elkington, S. R. (2013). Science goals and overview of the radiation belt storm probes (RBSP) energetic particle, composition, and thermal plasma (ECT) suite on NASA's Van Allen probes mission. *Space Science Reviews*, 179(1-4), 311-336. doi:10.1007/s11214-013-0007-5

Tanskanen, E. I. (2009). A comprehensive high-throughput analysis of substorms observed by IMAGE magnetometer network: Years 1993–2003 examined. *Journal of Geophysical Research: Space Physics*, 114(A5). doi:10.1029/2008JA013682

Takahashi, K., Anderson, B. J., Ohtani, S. I., Reeves, G. D., Takahashi, S., Sarris, T. E., and Mursula, K. (1997). Drift-shell

splitting of energetic ions injected at pseudo-substorm onsets. *Journal of Geophysical Research: Space* Physics, 102(A10), 22117-22130. doi:10.1029/97JA01870

Turner, D. L., Claudepierre, S. G., Fennell, J. F., O'Brien, T. P., Blake, J. B., Lemon, C., ... and Breneman, A. (2015). Energetic electron injections deep into the inner magnetosphere associated with substorm activity. *Geophysical Research Letters,* 42(7), 2079-2087. doi.org/10.1002/2015GL063225

Turner, D. L., Kilpua, E. K. J., Hietala, H., Claudepierre, S. G., O'Brien, T. P., Fennell, J. F., ... and Spence, H. E. (2019). The response of Earth's electron Statistics from the Van Allen Probes era including effects from different storm drivers. *Journal of Geophysical Research*: *Space Physics*, 124(2), 1013-1034. doi.org/10.1029/2018JA026066

Turner, N. E., Cramer, W. D., Earles, S. K., and Emery, B. A. (2009). Geoefficiency and energy partitioning in CIR-driven and CME-driven storms. *Journal of Atmospheric and Solar-Terrestrial Physics,* 71(10-11), 1023-1031. doi.org/10.1016/j.jastp.2009.02.005

Zheng, Y., Fok, M. C., and Khazanov, G. V. (2003). A radiation belt-ring current forecasting model. *Space Weather*, 1(3), 1-10. doi:10.1029/2003SW000007

Superposed epoch analysis